

# UBVRI twilight sky brightness at ESO-Paranal <sup>★</sup>

F. Patat<sup>1</sup>, O.S. Ugolnikov<sup>2</sup>, and O.V. Postlyakov<sup>3</sup>

<sup>1</sup> European Southern Observatory (ESO), K. Schwarzschildstr. 2, D-85748, Garching b. München, Germany  
e-mail: fpatat@eso.org

<sup>2</sup> Space Research Institute, Russian Academy of Sciences, Profsoyuznaya ul., 84/32, Moscow, 117997 Russia  
e-mail: ugol@tanatos.asc.rssi.ru

<sup>3</sup> A.M.Obukhov's Institute of Atmospheric Physics, Russian Academy of Sciences, Pyzhevsky per., 3, Moscow 119017 Russia  
e-mail: ovp@ifaran.ru

Received ...; accepted ...

## ABSTRACT

**Context.** Twilight studies have proved to be important tools to analyze the atmospheric structure with interesting consequences on the characterization of astronomical sites. Active discussions on this topic have been recently restarted in connection with the evaluation of Dome C, Antarctica as a potential astronomical site and several site-testing experiments, including twilight brightness measurements, are being prepared.

**Aims.** The present work provides for the first time absolute photometric measurements of twilight sky brightness for ESO-Paranal (Chile), which are meant both as a contribution to the site monitoring and as reference values in the analysis of other sites, including Dome C.

**Methods.** The *UBVRI* twilight sky brightness was estimated on more than 2000 FORS1 archival images, which include both flats and standard stars observations taken in twilight, covering a Sun zenith distance range 94°-112°.

**Results.** The comparison with a low altitude site shows that Paranal *V* twilight sky brightness is about 30% lower, implying that some fraction of multiple scattering has to take place at an altitude of a few km above the sea level.

**Key words.** atmospheric effects – site testing – techniques: photometric

## 1. Introduction

The quality of an astronomical site is determined by several parameters, which may vary according to the wavelength range of interest. For the optical and near-IR domain, these include typical seeing, sky transparency, number of clear nights, humidity, night sky brightness, amount of precipitable water vapor, dust and aerosols. While the seeing, extinction, sky brightness and other quantities are commonly measured at most observatories, the twilight brightness is not. This is mainly because the relevant information on the typical atmospheric conditions can be derived from other measurements obtained during the night. Nevertheless, twilight observations provide an independent tool for probing the overhead atmosphere under much higher flux conditions, thus allowing more accurate results. The interested reader can find an extensive review on this topic in the classical textbook by Rozenberg (1966).

Very recently, the twilight has received particular attention due to the growing interest of the international astronomical

community for what seems to be the new frontier of ground-based astronomy, i.e. Dome C - Antarctica. This site is exceptional under many respects. Besides the extremely good seeing conditions reported by Lawrence et al. (2004), several studies have shown very low amounts of precipitable water vapor which, coupled to a low sky emission, could imply that this is the best site for IR and sub-millimetric ground-based astronomy. A review about the characteristics of Dome C has been recently presented by Kenyon & Storey (2005).

One of the main concerns is related to the high latitude of this site. This, in fact, causes a significant reduction in the amount of dark time with respect to equatorial observatories, thus posing some doubts about the effective exploitation of the exceptional seeing in the optical. The possibility of opening spectral windows otherwise inaccessible from the ground is in itself a valid and sufficient scientific driver for Dome C. Nevertheless, arguments in favor of Dome C as a site for optical astronomy have been put forward. Among these, a smaller average contribution by the scattered moonlight to the global background and a cleaner atmosphere have been advocated as features that may possibly compensate for the reduced dark time (Kenyon & Storey 2005). In particular, since the last

---

Send offprint requests to: F. Patat

<sup>★</sup> Based on observations made with ESO Telescopes at Paranal Observatory.

phases of twilight (also known as deep twilight) are dominated by multiple scattering (Rozenberg 1966), the amount of scattered sunlight is strongly dependent on the amount of aerosol in the lower atmospheric layers (see for example Ougolnikov et al. 2004). In a supposedly low aerosol content site like Dome C, this effect is expected to be very low and this, in turn, would allow one to start the observations earlier than at *normal* sites. Even though the argument has a good physical ground, direct on site measurements are still lacking. In this respect, it is worth mentioning that a couple of dedicated experiments for sky brightness measurements are currently being setup (A. Moore, J. Storey 2006, private communications).

In spite of the large number of investigations done in the past in this field, absolute twilight brightness measurements are rather rare, especially for large observatories placed in top rated sites. To our knowledge, the only published work on twilight observations in the Johnson-Cousins standard system is the one by Tyson & Gal (1993) who however, given their purposes, report only uncalibrated data for CTIO. In the light of these fact, both with the purpose of characterizing Paranal also from this new point of view and to provide the community with absolute reference values obtained over a large time baseline, we present here for the first time *UBVRI* twilight sky brightness measurements.

The paper is organized as follows. In Sec. 2 we introduce the basic concepts through a simplified model (which is discussed in more detail in Appendix A), while in Sec. 3 we describe the observations, data reduction and calibration. The *UBVRI* twilight sky brightness measured at ESO-Paranal is presented and discussed in Sec. 4, while Sec. 5 summarizes the results obtained in this work.

## 2. The twilight problem

The calculation of scattered flux during twilight is a rather complicated problem that requires a detailed treatment of multiple scattering (see for example Blättner et al. 1974 and Wu & Lu 1988) and an accurate description of the atmospheric composition and the physical phenomena taking place in the various layers (Divari & Plotnikova 1966; Rozenberg 1966). Notwithstanding the large amount of work done in the '60 and in the '70, the problem is still matter of investigations (see for example Anderson & Lloyd 1990; Ougolnikov 1999; Ougolnikov & Maslov 2002; Ekstrom 2002; Ougolnikov, Postlyakov & Maslov 2004; Postlyakov 2004; Mateshvili et al. 2005). While it is well beyond the purposes of the present work to explore the problem from a theoretical point of view, we deem it is interesting to introduce a simple single-scattering model, which is useful both to understand the basic principles of twilight and to provide a quick comparison to the observed data. The assumptions and the model itself are discussed in Appendix A, to which we refer the interested reader for the details, while here we concentrate on the model predictions only.

The calculated zenith ( $\alpha=0$ ) *UBVRI* sky brightness as a function of Sun zenith distance  $\zeta$ , computed using the average broad band extinction coefficients for Paranal (Patat 2003a), are plotted in Fig. 1. As one can immediately see, the single scattering component drops below the night sky brightness be-

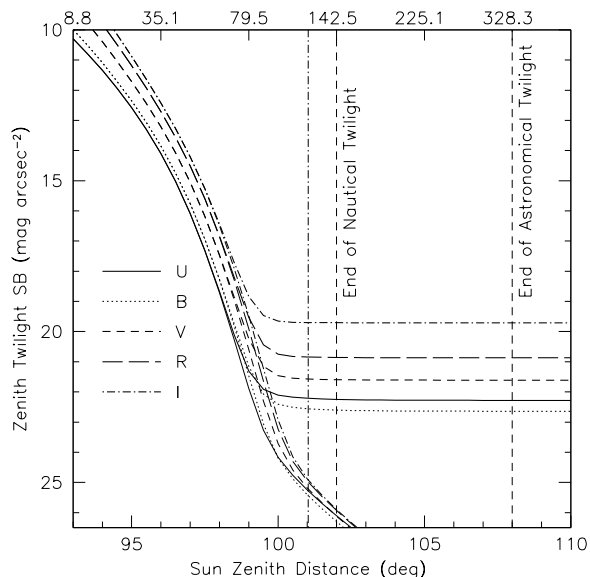


**Fig. 1.** Model twilight sky brightness at zenith. The thick curves include the night sky contribution, while the thin lines indicate the scattered component only. The vertical dashed-dotted line marks the Sun zenith distance when the lower boundary layer height is 120 km. The upper scale indicates the lower Earth's boundary layer height in km.

tween  $\zeta=99^\circ$  and  $\zeta=100^\circ$ , indicating that from this point on multiple scattering is the only contributor to the observed flux, as shown by Ugolnikov & Maslov (2002) on the basis of polarization measurements.

Another aspect to be considered is the fact that the transition to the flatter part of the atmospheric density profile (see Fig. A.2) definitely occurs during the multiple scattering-dominated phase. Since multiple scattering takes place with higher probability where the density is higher, i.e. in the lower atmospheric layers, the explanation given by Tyson & Gal (1993) for the observed brightness decline rate during twilight does not seem to be correct. In fact, these authors interpret the observed values as the pure consequence of the lower shadow boundary height change, neglecting extinction and multiple scattering. They conclude that, since their observations have been taken when  $100 \leq h_z \leq 400$  km (where  $h_z$  is the height of the lower Earth's shadow boundary along the zenith direction; see also Appendix A), the sky brightness rate is directly related to the slope of the density law in that region of the atmosphere. Nevertheless, the calculation of Sun's ephemeris for the site and epoch of Tyson & Gal's observations shows that, in the most extreme case (see their Table 1, *R* filter), it was  $1^\circ.8 \leq \varphi \leq 7^\circ.4$  (where  $\varphi = \zeta - 90$ ). As the reader can figure out from Table A.1, this implies that  $h_z < 80$  km in all cases, i.e. well within the steep part of the density profile. Therefore, the fact that the observed rate and the rate expected from pure single scattering in the higher atmospheric layers are consistent, is just a coincidence.

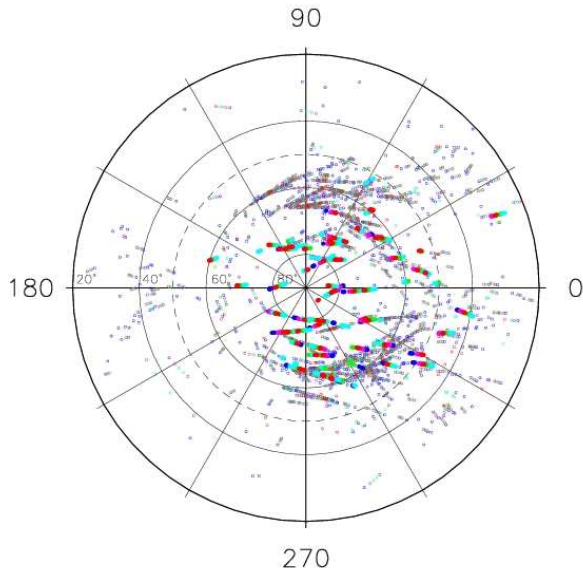


**Fig. 2.** Distribution of twilight observations in Alt-Az coordinates for TSF (filled symbols) and LSE (empty symbols). The astronomical azimuth has been replaced with the difference in azimuth between the telescope pointing and the Sun,  $\Delta\alpha_{\odot}$ .

### 3. Observations, Data Reduction and Calibration

In order to measure the twilight sky brightness on Paranal, we have used archival calibration data obtained with the FOcal Reducer/low dispersion Spectrograph (hereafter FORS1), mounted at the Cassegrain focus of ESO–Antu/Melipal 8.2m telescopes (Szeifert 2002). The instrument is equipped with a  $2048 \times 2048$  pixels (px) TK2048EB4-1 backside thinned CCD and has two remotely exchangeable collimators, which give a projected scale of  $0''.2$  and  $0''.1$  per pixel ( $24\mu\text{m} \times 24\mu\text{m}$ ). According to the used collimator, the sky area covered by the detector is  $6'.8 \times 6'.8$  and  $3'.4 \times 3'.4$ , respectively. For this study we have selected only the data obtained with the lower resolution collimator and the 4-port high-gain read-out mode, since this combination is the most used for imaging with FORS1. With this setup the read-out noise is 5.5 electrons ( $e^-$ ).

For our purposes, we have selected two sets of data. The first is composed by broad-band *UBVRI* twilight sky flats (hereafter TSF), which are regularly obtained as part of the calibration plan. In the current implementation, after taking a test exposure the observing software estimates with a simple algorithm the integration time for the first exposure in a series of 4 frames. Subsequent exposure times are adjusted on the basis of the previous exposure level and this allows one to obtain high signal-to-noise images with a rather constant counts level, which is typically around 20,000 ADUs. This is achieved with exposure times which range from 0.25 sec up to 5 minutes. Given these values, the sensitivity of FORS1 in the various passbands and the typical twilight sky brightness behaviour (see for example Fig. 1), these observations are expected to approximately cover the Sun zenith distance range  $94^\circ \leq \zeta \leq 101^\circ$ , i.e. still within the nautical twilight. Since the most important part of this analysis concerns the deep twilight, it is

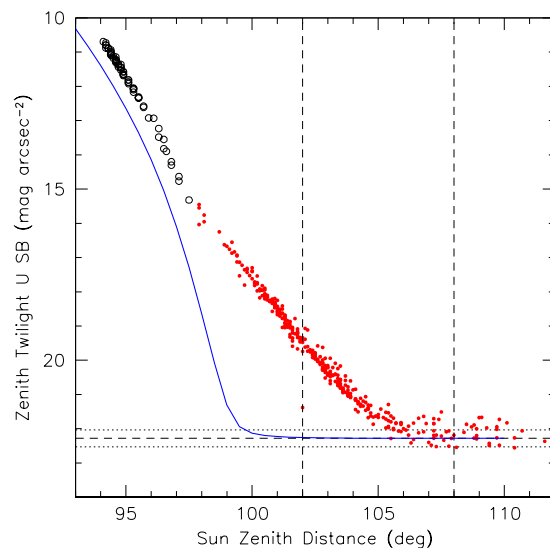


**Fig. 3.** Zenith twilight sky surface brightness in the *U* passband from TSF (empty symbols) and LSE (filled symbols) with  $|\alpha| \leq 40^\circ$ . The vertical dashed lines mark the end of nautical (left) and astronomical (right) twilight. The solid curve traces the simple model described in the text. The horizontal lines indicate the *U* dark time night sky brightness average value (dashed) for Paranal (Patat 2003a) and the  $\pm 1\sigma$  levels (dotted).

clear that an additional set of data is required to complement the sky flats.

The calibration plan of FORS1 includes the observation of standard stars fields (Landolt 1992) in *UBVRI* passbands, which are regularly taken during twilight, typically just after the sky flats sequence is completed. For calibration purposes, a fraction of these exposures are obtained using relatively long integration times (typically 40 sec for *U* and 20 sec for *BVRI*) which, at an 8 m-class telescope, are sufficient to bring the sky background at exposure levels which are suitable to our purposes. In fact, the bulk of these observations covers the range  $100^\circ \leq \zeta \leq 112^\circ$ , i.e. well into astronomical twilight. For the sake of clarity we will indicate them as long exposure standards (LES).

In order to collect a statistically significant sample, we have retrieved from the ESO Archive all suitable TSF obtained in *UBVRI* passbands from 01-01-2005 to 30-09-2005, for a total of 1083 frames (*U*: 148, *B*: 208, *V*: 226, *R*: 261, *I*: 240). Since a much higher night-to-night spread is expected in the deep twilight phase due to the natural fluctuations of the night sky emission and also because LSE are less frequently obtained than TSF, a larger time interval must be considered. To this aim, we have put together the LES sample collecting all suitable images obtained from 01-01-1999 (i.e. shortly after the beginning of FORS1 operations) to 30-09-2005, thus covering almost 6 years, for a total of 3388 frames (*U*: 923, *B*: 611, *V*: 609, *R*: 635, *I*: 610). All images were processed within the *xccdred* package of IRAF<sup>1</sup>. Due to the large amount of data and the

<sup>1</sup> IRAF is distributed by the National Optical Astronomy Observatories, which are operated by the Association of Universities

purpose of this work, the bias subtraction was performed using a pre-scan correction only, while flat-fielding was achieved using a stack of all TSF in each given passband as a master flat, which was then adopted to correct each TSF and LES frame.

Due to the nature of the data, there is no need for taking care of the possible presence of crowded stellar fields or bright extended objects, as it is the case for night sky brightness estimates (see Patat 2003b). For this reason, the background in each image was measured using a simple and robust mode estimator. To avoid possible vignetting and flat fielding problems, only the central  $1024 \times 1024$  pixels were considered. On these spatial scales and due to improper flat-fielding, FORS1 is known to show variations of the order of a few percent, while the gradients in the twilight sky are much smaller (see Chromey & Hasselbacher 1996) and can be safely neglected. Therefore, the mode  $\langle I \rangle$  of pixel intensity distribution is assumed as the best estimate of the sky background. For each filter, this is converted into a surface brightness in the Johnson-Cousins system via the following relation

$$b = -2.5 \log \langle I \rangle + 2.5 \log(p^2 t_{exp}) + m_0$$

where  $p$  is the pixel scale ( $\text{arcsec px}^{-1}$ ),  $t_{exp}$  is the exposure time (seconds) and  $m_0$  is the instrumental photometric zero-point for the given passband. No color correction has been applied, for two reasons: a) colour terms in FORS1 are very small (Patat 2003a); b) color correction depends on the intrinsic color which, for the twilight sky, changes according to time and position. Given this and the fact that night-to-night fluctuations are the dominating source of noise in the measurements, the color correction can be safely neglected. As for the instrumental zero-points, we have used the average values computed for the period of interest using data taken during photometric nights only. Variations in the zero-points are known to take place (Patat 2003a), mainly due to the aging of telescope reflective surfaces but, again, these are smaller than the inherent sky variations. Finally, no airmass correction has been applied and this is expected to produce an additional spread in the data close to the end of astronomical twilight and a systematic increase in the average sky brightness in that region. Due to the large number of pixels used ( $N > 10^6$ ), the typical internal photometric error is expected to be less than 1%.

#### 4. Twilight sky brightness at ESO-Paranal

Not being obtained specifically for twilight brightness measurements, the data are inhomogeneously distributed on the sky. In fact, in an Alt-Az plot where the ordinary azimuth is replaced by the difference in azimuth between the sky patch and the Sun ( $\Delta a_\odot \equiv a - a_\odot$ ), the data points tend to cluster in two regions, which correspond to evening and morning observations (Fig. 2). Besides target azimuth and altitude, for each data point we have computed a series of other quantities, which are relevant for the subsequent analysis. These include Sun azimuth and altitude, Sun-target angular separation, Moon phase, Moon altitude and Moon-target angular separation. To avoid

for Research in Astronomy, under contract with the National Science Foundation.

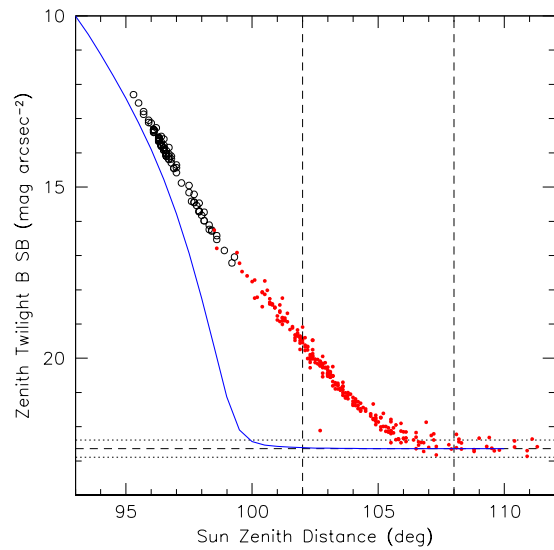


Fig. 4. Same as Fig. 3 for the  $B$  passband.

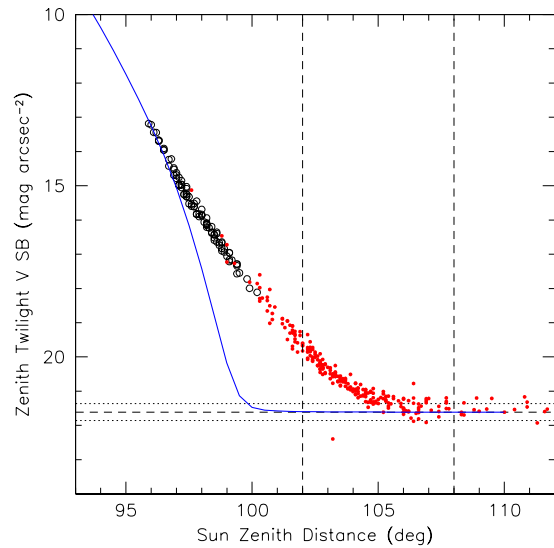


Fig. 5. Same as Fig. 4 for the  $V$  passband.

contamination from scattered moonlight in the LSE, we have selected only those data points for which the Moon was below the horizon.

Since the twilight sky brightness for a given Sun zenith distance changes with the position on the sky, in order to study its behavior as a function of  $\zeta$  it is necessary to make a selection on the Alt-Az coordinates. Given the nature of the available data, which appear to be rather concentrated (Fig. 2), it seems reasonable to restrict the analysis to zenith region only. In order to have a sufficient amount of measurements, we have used all data points with zenith distance  $|\alpha| \leq 40^\circ$ , which is of course expected to cause some additional spread in the observed relation. The results are presented in Figs. 3-7 for the  $UBVRi$  passbands respectively.

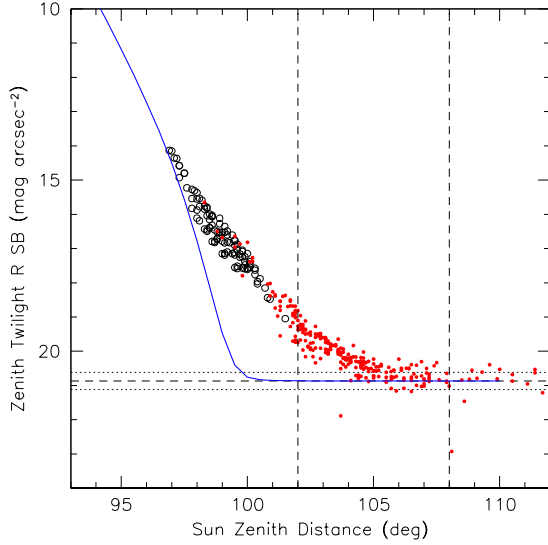


Fig. 6. Same as Fig. 3 for the *R* pass band.

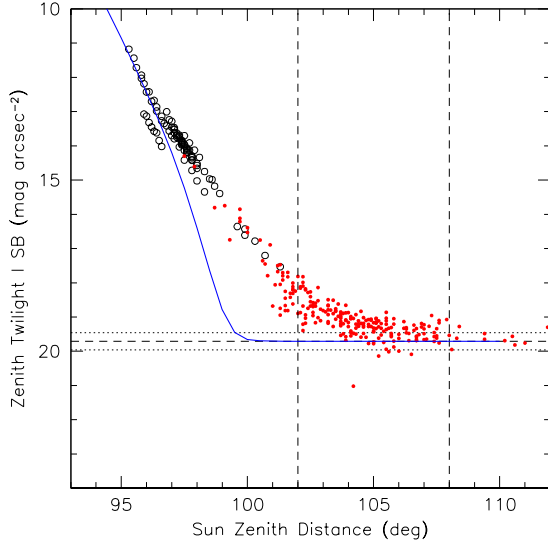
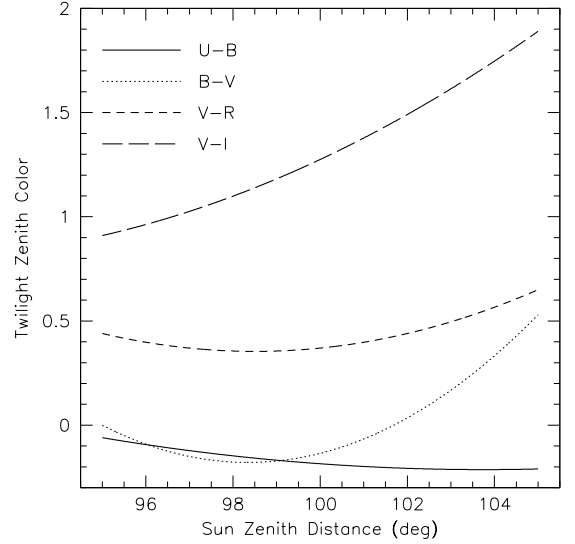


Fig. 7. Same as Fig. 3 for the *I* passband.

As expected, the single scatter model drops much faster than the actual observations. Whilst for *VRI* the model deviates from the data around  $\zeta \sim 97^\circ$ , for *B* and especially for *U* the model underestimates the surface brightness already at  $\zeta \leq 96^\circ$ , indicating that multiple scattering is more efficient at shorter wavelengths. This is in agreement with the findings of Ougolnikov & Maslov (2002), who have shown that the contribution of single scattering in the phases immediately following sunset is about 40%, 60%, 70% and 80% in *U*, *B*, *V* and *R* respectively. These fractions remain roughly constant until  $\zeta \leq 95^\circ$ , after which the role of single scattering becomes weaker and weaker and multiple scattering takes rapidly over. In all passbands, the night sky brightness level is reached at around  $\zeta = 105^\circ - 106^\circ$ .

**Table 1.** Twilight sky brightness fitted parameters in the range  $95^\circ \leq \zeta \leq 105^\circ$ . All values are expressed in  $\text{mag arcsec}^{-2}$ .

Filter	$a_0$	$a_1$ $\text{deg}^{-1}$	$a_2$ $\text{deg}^{-2}$	$\sigma$	$\gamma$ $\text{deg}^{-1}$
U	11.78	1.376	-0.039	0.24	$1.23 \pm 0.01$
B	11.84	1.411	-0.041	0.12	$1.24 \pm 0.01$
V	11.84	1.518	-0.057	0.18	$1.14 \pm 0.02$
R	11.40	1.567	-0.064	0.29	$1.09 \pm 0.03$
I	10.93	1.470	-0.062	0.40	$0.94 \pm 0.03$



**Fig. 8.** Broad band zenith twilight sky colors. The curves have been computed using second order polynomials fitted to the observed data. For comparison, the colors of the Sun are  $U - B = 0.13$ ,  $B - V = 0.65$ ,  $V - R = 0.52$  and  $V - I = 0.81$ , while those of the night sky at Paranal are  $U - B = -0.36$ ,  $B - V = 1.03$ ,  $V - R = 0.74$  and  $V - I = 1.90$  (Patat 2003a).

In order to give a more quantitative description of the observations, we have fitted the surface brightness data in the range  $95^\circ \leq \zeta \leq 105^\circ$  using second order polynomials of the form  $a_0 + a_1(\zeta - 95) + a_2(\zeta - 95)^2$ , with  $\zeta$  expressed in degrees and the surface brightness in  $\text{mag arcsec}^{-2}$ . The results are presented in Table 1, where we have reported also the RMS deviation from the fitted function  $\sigma$  and the slope  $\gamma$  deduced from a linear fit to the data in the range  $95^\circ \leq \zeta \leq 100^\circ$ , i.e. during the interval typically used to obtain TSF exposures, when the contribution by the night sky is still moderate. A first aspect to be noticed is the spread shown by the data points around the mean laws, which are due to the night-to-night variations in the atmospheric conditions. The dispersion becomes particularly large in the *I* passband, where the fluctuations appear to be quite pronounced. As for the decay rate during nautical twilight, we notice that this tends to decrease for increasing values of wavelength.

To convert the values of  $\gamma$  reported in Table 1 into surface brightness variation per unit time, one has to multiply them by  $d\phi/dt$ , which is given by:

$$\frac{d\phi}{dt} = \cos \varphi \sin H_\odot \cos \delta_\odot \cos \phi \frac{dH_\odot}{dt}$$

where  $H_{\odot}$  and  $\delta_{\odot}$  are the hour angle and declination of the Sun respectively, while  $\phi$  is the site latitude (see for example Smart 1977). Since  $dH_{\odot}/dt \approx 0.25 \text{ deg min}^{-1}$ , for  $\phi \sim 0$  (i.e. at the time of sunrise and sunset) for Paranal ( $\phi = -24.6$ ) one obtains  $d\phi/dt = 0.23 \text{ deg min}^{-1}$  at the equinoxes ( $\delta_{\odot} = 0$ ). Applying this factor to the values reported in the last column of Table 1, one obtains brightness decline rates that range from 0.28 ( $U$ ) to 0.22 ( $I$ )  $\text{mag arcsec}^{-2} \text{ min}^{-1}$ . These values can be directly compared with those reported by Tyson & Gal (1993). The data available to these authors did not allow them to quantify the differences between the various filters and hence they report a mean value of  $\gamma = 0.23 \pm 0.02 \text{ mag arcsec}^{-2} \text{ min}^{-1}$  which is within the range defined by our data.

With the aid of the second order best fit relations, we have computed the color curves presented in Fig. 8. Due to the dispersion of the observed data, these colors have to be regarded only as indicative, especially in the region  $\zeta > 102^{\circ}$ , where the inherent night sky brightness fluctuations start to be significant, particularly in the red passbands. It is interesting to note that while  $U - B$  and  $V - R$  colors do not change very much as the Sun sinks below the horizon, significant changes take place in  $B - V$  and especially in  $V - I$ . In principle one expects that since multiple scattering boosts the light at shorter wavelengths with respect to the pure single scattering component, the overall color gets bluer and bluer as the Sun deepens below the horizon. Then, at some point, the night sky glow which has completely different colours, starts to contribute and the colors progressively turn to those typical of the night sky. As a matter of fact, the observed  $U - B$ ,  $B - V$  and  $V - R$  curves indeed show this behaviour (see Fig. 8), while  $V - I$  turns steadily redwards. This is due to the interplay between input Sun spectrum, scattering efficiency, extinction, multiple scattering and the emergence of the night glow, which combine together in quite a complicated way. This is clearly illustrated in Fig. 9, where we present twilight spectra obtained on Paranal with FORS1 and his twin instrument FORS2. The sky spectra were extracted from spectrophotometric standard stars observations taken during twilight (see Table 2) and were wavelength and flux calibrated with standard procedures in IRAF. The exposure times ranged from 10 sec to 120 seconds and the signal-to-noise ratio was increased meshing all pixels in the direction perpendicular to the dispersion, after removing the region of the detector affected by the well exposed standard star spectrum. For comparison, Fig. 9 shows also the typical dark time spectrum of Paranal (Patat 2003a) and the solar spectrum.

With the exception of the first spectrum, which was obtained with a very low resolution ( $\sim 130 \text{ \AA}$  FWHM), the remaining data allow one to detect quite a number of details. For  $\phi < 12^{\circ}$ , i.e. during the nautical twilight, the spectrum is rather different from that of the Sun, even though it shows clear solar features, like the CaII H&K lines and the G-band at about 4300  $\text{\AA}$ . The Rayleigh scattered Sun flux gives a clear contribution in the region bluewards of 5000  $\text{\AA}$  down to  $\phi = 15^{\circ}$ , after which the pseudo-continuum of the night sky emission takes over.

For  $\phi < 9^{\circ}$ , the contribution by night sky emission lines is very weak. Characteristic lines like [OI]5577  $\text{\AA}$  and [OI]6300,6364  $\text{\AA}$  (the latter overimposed on a  $\text{O}_2$  absorption band) are barely visible, while the OH Meinel bands start

**Table 2.** Basic data for twilight sky spectra shown in Fig. 9.

Date	UT start	$\Delta\lambda/\lambda$ $\text{\AA}(\text{FWHM})$	Alt deg	Az deg	$\phi$ deg
2001-09-21	10:06:58	130	82.6	117.5	6.5
2003-11-29	09:02:25	13	65.8	122.9	9.4
2003-02-28	09:45:52	16	27.5	299.3	11.9
1999-04-16	09:54:36	12	41.1	233.4	14.8

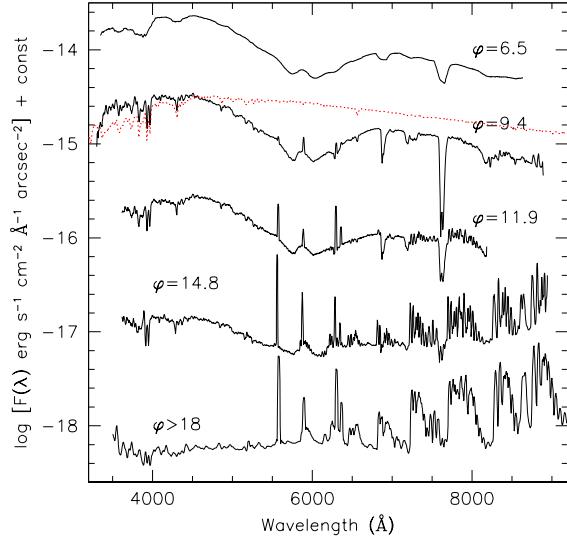


**Fig. 9.** Twilight spectra obtained at Paranal at different Sun depression angles. For convenience, the spectra have been corrected to the corresponding  $V$  flux shown by the photometric data. Spectral resolution and sky patch differ from spectra to spectra (see Table 2). For presentation the spectra have been vertically shifted by the following amounts: +0.50 ( $\phi = 9.4$ ), +0.35 ( $\phi = 11.9$ ), -0.10 ( $\phi = 14.8$ ), -1.0 ( $\phi > 18$ ). The dotted line traces the solar spectrum, normalized to the continuum of the  $\phi = 9.4$  spectrum at 4500  $\text{\AA}$ .

to appear above 8000  $\text{\AA}$ . One remarkable exception are the NaI D lines, which are known to be present during the so called *sodium flash* (Rozenberg 1966). A similar phenomenon is present for the [OI]6300,6364  $\text{\AA}$  doublet (see for example Roach & Gordon 1973), which is indeed visible in Fig. 9 already at  $\phi = 9.4$ . With the onset of astronomical twilight, the spectrum in the red is more and more dominated by the OH bands. Another remarkable fact is the behaviour of the  $\text{H}_2\text{O}$  (6800, 7200  $\text{\AA}$ ) and  $\text{O}_2$  (7600  $\text{\AA}$ ) molecular absorption bands. During the bright twilight, when single scattering is still relevant ( $\phi = 6.5$ ), they already appear to be significant, but they become even deeper in the multiple scattering-dominated phase ( $\phi = 9.4$ ), due to the longer optical path traveled by the multiply scattered photons. For higher values of  $\phi$  they progressively disappear due to the weakening of the scattered Sun's continuum.

In order to estimate the effects of site altitude on the twilight sky brightness, we have compared the results presented here with data obtained at the Southern Laboratory of the Sternberg Astronomical Institute (Moscow, Russia) during three morning twilights on December 9-11, 2002 (see Fig. 10). This facility is

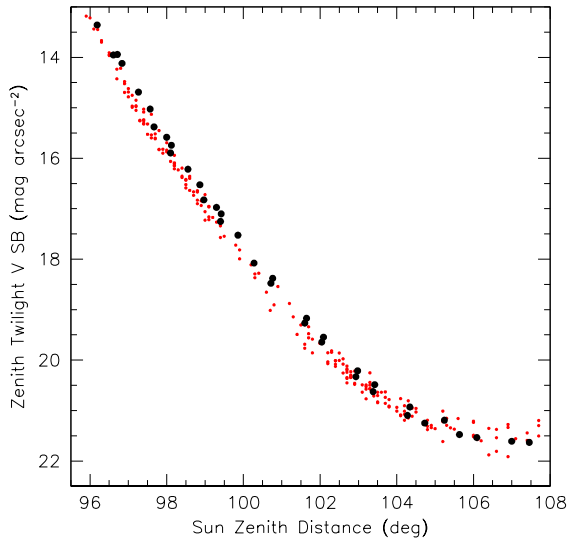


**Fig. 10.** Comparison between the zenith twilight sky brightness measured on Paranal (small symbols) and Crimean Astrophysical Observatory (large symbols) for the V passband.

located within the Crimean Astrophysical Observatory (CrAO), at a latitude of  $44.7^\circ$  North and 600 m a.s.l.. The observations were performed using a wide-field CCD-camera with a field of view of  $8^\circ \times 6^\circ$  and exposure times that ranged from 0.01 to 18 seconds. Photometric calibration was achieved using field stars included in the Tycho-2 Catalog (Hog et al. 2000). The photometric passband of this instrument is fairly similar to the Johnson-Cousins V, with a colour correction of the order of 0.01 mag for the  $(B - V)$  colour range shown by twilight data.

The two data sets clearly show that the twilight background at CrAO is systematically brighter; the difference is constant during the dark twilight period and vanishes at nightfall. More precisely, the comparison between V band data in moonless conditions at CrAO (zenith) and ESO-Paranal ( $|\alpha| \leq 20^\circ$ ) shows that the mean difference in the Sun depression range  $5.5^\circ \leq \varphi \leq 11.0^\circ$  is  $\Delta V = 0.27 \pm 0.03$ . On the other hand, the typical atmospheric pressure value for ESO-Paranal is  $P_1 = 743$  hPa, and for CrAO during the observations  $P_2 = 961$  hPa. Interestingly, the magnitude difference implied by the pressure ratio at the two sites is  $-2.5 \log(P_1/P_2) = 0.28$ , which is indeed very similar to the measured difference  $\Delta V$ . Therefore, we can conclude that the deep twilight sky brightness is proportional to the atmospheric pressure or, equivalently, to the atmospheric column density above the observer. In turn, this implies that the light undergoes multiple scattering throughout the whole atmosphere and not only in the upper layers. Given that the difference in altitude between Paranal and CrAO is only 2 km, the observations we present here suggest that some fraction of multiple scattering has to take place in the first few km above the sea level.

## 5. Discussion and Conclusions

In this paper we have presented for the first time absolute UVBRI twilight brightness measurements for the ESO-Paranal Observatory (Chile) spanning almost 6 years. These measurements will serve as reference values for the similar studies which will be soon conducted at Dome C, Antarctica, as part of the site testing campaign. The planned *in situ* spectrophotometric measurements will finally clarify whether this exceptional location shows a lower aerosols content, as expected both due to the icy soil and to its large distance from the sea coast (Kenyon & Storey 2005).

The twilight sky brightness measurements presented here were obtained from VLT-FORS1 archival data not specifically taken for this kind of studies. Also, due to the large telescope diameter, the initial twilight phases ( $0^\circ \leq \varphi \leq 6^\circ$ ) are not covered. In a sense this is quite unfortunate, since for these low Sun depression angles the lower shadow's boundary passes through the atmospheric layers below  $\sim 30$  km (see Table A.1), where the ozone and aerosol stratospheric concentration is maximum. These phases are in fact used to retrieve ozone and aerosol profiles, using both intensity and polarization measurements (see for example Wu & Lu 1988; Ugolnikov et al. 2004; Mateshvili et al. 2005). Nevertheless, during the deep twilight, when the direct Sun radiation illuminates only the upper atmospheric layers and single scattering on air molecules becomes progressively less important, the amount of aerosols and ozone plays a relevant role through multiple scattering. Therefore, even though of much more complicated interpretation, deep twilight observations may still give some insights on the conditions in the lower atmosphere. Moreover, in the context of the discussion about the supposedly shorter twilight duration at Dome C (see Kenyon & Storey 2005), what really matters is the behavior during the deep twilight. An example of this kind of analysis is shown in Fig. 11, where the data obtained at Paranal are compared to the MCC++ model calculations for a site at 2.6 km a.s.l. (see Postlyakov 2004 for a detailed description). This code treats the radiative transfer in a spherical atmosphere including Ozone, Aerosol and molecular scattering, also taking into account the backscattering by the Earth's surface. As one can see the overall behavior is fairly well reproduced. The deviations are possibly due to the differences in real and model aerosol, since multiple scattering is very sensitive to it. The model adopts a urban microphysical model for the first 10 km of the atmosphere and this is certainly different from what is expected for a desertic area close to the sea, as is the case of Paranal. Dedicated instruments for twilight sky brightness monitoring coupled to detailed modeling may indeed give a useful contribution to the already existing site testing tools, providing independent indications about the overhead aerosol profile.

Some interesting results are obtained comparing the estimates obtained for Paranal (2600 m a.s.l.) with those of a significantly lower site like CrAO (600 m a.s.l.). Despite the fact that the bright twilight and night sky brightnesses are very close at the two sites, during the deep twilight Paranal is about 30% darker than CrAO in the V passband (see Fig. 10). Due to the higher altitude, Paranal suffers from a lower extinction



gle  $\theta = \pi/2 - \alpha + \varphi$ . according to the scattering phase function  $\Phi(\theta)$ , which obeys to the usual normalization condition

$$\int_{4\pi} \Phi(\theta) d\Omega = 1 \quad (\text{A.1})$$

Before reaching the observer, it undergoes the extinction along  $OP$ . The total flux will finally result from the integration along the illuminated segment  $P_0P_1$ . In order to compute the required quantities, we must first derive a series of useful relations. Since one has to evaluate the particle density along the generic light path, it is fundamental to know the height  $h = GP$  above the sea level for any given point along the trajectory. This is particularly simple for the travel between  $O$  and  $P_1$ , for which one can easily derive the following relation:

$$h_{OP_1} = \sqrt{l^2 + 2l(R_0 + h_s) \cos \alpha + (R_0 + h_s)^2} - R_0 \quad (\text{A.2})$$

where  $l$  is the coordinate along  $OP_1$  ( $l=0$  in  $O$ ). Another useful relation is the one that gives the lower limit for the integral along the line of sight, i.e. the optical path  $l_0$  between  $O$  and  $P_0$ . In order to get the required expression, one first needs to find the length of  $H_0P_0$  and  $h_0$ , i.e. the height above the sea level of  $P_0$ . These can be obtained after some trigonometry and are respectively

$$H_0P_0 = R_0 \left[ \tan \varphi - \frac{\sin \alpha}{\cos(\alpha - \varphi)} \left( \frac{1 - \cos \varphi}{\cos \varphi} - \frac{h_s}{R_0} \right) \right]$$

and

$$h_0 = \sqrt{H_0P_0^2 + R_0^2} - R_0$$

Having these two equations at hand, one can easily find  $l_0$ :

$$l_0 = \frac{\sqrt{(R_0 + h_s)^2 \cos^2 \alpha + h_0^2 - h_s^2 + 2R_0(h_0 - h_s)} - (R_0 + h_s) \cos \alpha}{\cos \alpha}$$

As for the upper limit  $l_1$  along the line of sight, this turns out to be:

$$l_1 = \frac{\sqrt{(R_0 + h_s)^2 \cos^2 \alpha + 2R_0(\Delta R - h_s) + \Delta R^2 - h_s^2} - (R_0 + h_s) \cos \alpha}{\cos \alpha}$$

The next step is the calculation of  $h_{QP}$ , the height along the sun ray. In order to do so, we introduce the perigee height  $\delta$ , i.e. the minimum distance between the Earth's surface and the sun ray passing through  $P$ , which can be expressed as a function of the  $l$  coordinate along  $P_0P_1$  as follows:

$$\delta = (l - l_0) \cos(\alpha - \varphi)$$

Having this in mind, one can derive the length of  $QH$  as follows:

$$QH = \sqrt{2R_0(\Delta R - \delta) + \Delta R^2 - \delta^2}$$

If we then introduce a coordinate  $q$  along  $QP$  (with  $q=0$  in  $Q$ ), considering the fact that  $(QH - q)^2 + (R_0 + \delta)^2 = (R_0 + h)^2$ , we finally obtain

$$h_{QP} = \sqrt{(QH - q)^2 + (R_0 + \delta)^2} - R_0 \quad (\text{A.3})$$

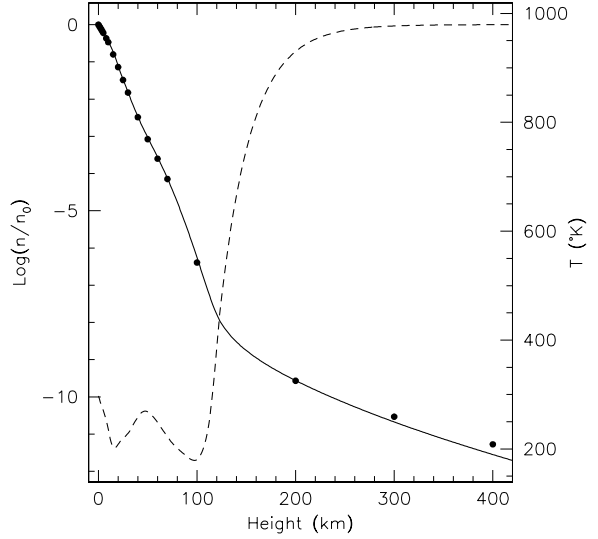


**Fig. A.2.** Normalized density (solid line) and temperature (dashed line) profiles according to the MSIS-E-90 model (Hedin 1991). For comparison, the dots trace the values of the US Standard Atmosphere (McCartney 1976, Tab. 2.6).

**Table A.1.** Height of lower boundary of Earth's shadow at zenith ( $h_z$ ) and at  $60^\circ$  from zenith along the solar meridian in the Sun's direction.

$\varphi$ (deg)	$h_z$ (km)	$h_0(\alpha = 60)$ (km)
3	8.8	8.0
6	35.1	29.9
9	79.5	63.3
12	142.5	106.7
15	225.1	159.1
18	328.3	220.1

with  $0 \leq q \leq QP$ . The optical path of the unscattered sun ray  $QP$  is given by the sum of  $QH$  and  $HP$ , the latter being  $HP = H_0P_0 - (l - l_0) \sin(\alpha - \varphi)$ . By means of Equations A.2 and A.3 one can now compute the height above the sea level (and hence the particle number density) along the light path. The height along the zenith direction,  $h_z = TZ_0$ , can be readily derived and it is given by

$$h_z = R_0 \frac{1 - \cos \varphi}{\cos \varphi}$$

From this one can figure out how fast  $h_z$  grows when the sun depression  $\varphi$  increases (see also Tab. A.1). This, coupled to the rapid decrease of the atmospheric density as a function of height, is the cause for the very quick drop in the twilight sky surface brightness.

### A.3. Density profile and optical depth

As we have anticipated, for the density profile we have adopted the MSIS-E-90 model<sup>3</sup> density profile (Hedin 1991), which is

<sup>3</sup> <http://modelweb.gsfc.nasa.gov/models/msis.html>

presented in Fig. A.2. As the plot shows, the global profile can be roughly described by two laws: one exponential (for  $h < 120$  km, the so called homosphere) and a power law (for  $120 < h < 400$  km, the so called thermosphere). Clearly, as the Sun depression increases, the lower Earth's shadow boundary will pass through more and more tenuous atmospheric layers and, therefore, the change in density slope should turn into a change in the twilight sky surface brightness decline. Under the assumptions made for this simplified model, this should happen when  $\varphi \approx 101^\circ$ , i.e. close to the end of nautical twilight.

Since in the following section we will be interested in the product between the number density and the extinction cross section, we can derive this, for a given passband, assuming the measured extinction coefficient  $\kappa(\lambda)$  (in mag airmass<sup>-1</sup>) and integrating the previous density profile along the vertical (i.e. at airmass 1). In fact, assuming that all the extinction comes from Rayleigh scattering, one can write:

$$\tau_z(\lambda) = n_0 C_{ext}(\lambda) \int_{h_s}^{\Delta R} \frac{n(h)}{n_0} dh$$

Then, considering that  $\tau_z(\lambda) = 1.086\kappa(\lambda)$ , the product  $n_0 C_{ext}(\lambda)$  can be readily derived from the previous relation and used in all further optical depth calculations.

#### A.4. Scattering cross section and phase function

The  $\lambda^{-4}$  wavelength dependency of the Rayleigh scattering cross section is implicitly taken into account by the extinction coefficients, which are to be considered as input data to the model and not as free parameters. As for the scattering phase function we have used the canonical expression for air molecules (McCartney 1976):

$$\Phi(\theta) = \frac{3}{16\pi} [1 + 0.9324 \cos^2(\theta)]$$

where the multiplicative constant comes from the normalization condition expressed by Equation A.1.

#### A.5. Scattered flux

The scattered flux can be computed in the same way as done, for example, by Krisciunas & Schaefer (1991) for the Moon light. If  $L_\odot$  is the luminosity of the sun at a given wavelength (expressed in photons per unit time and per unit wavelength), the flux received by the Earth at the top of the atmosphere is  $F_\odot^0 = L_\odot/4\pi d^2$ , where  $d=1$  AU. If we now consider an infinitesimal volume element  $dV$  placed along the line of sight at a distance  $l$  from  $O$ , the number of scattered photons received by the observer per unit time, unit area and unit wavelength is given by

$$df = F_\odot^0 e^{-\tau(OP)} n[h(l)] C_{ext}(\lambda) \frac{\Phi(\theta)}{l^2} e^{-\tau(OP)} dV \quad (\text{A.4})$$

Given the geometry of the problem, the infinitesimal volume element can be written as  $dV = dS dl \equiv \pi l^2 \phi^2 dl$ , where  $\phi$  is the semi-amplitude of the angle subtended by  $dS$  at the distance of the observer. Since the solid angle subtended by  $dS$

is  $d\Omega = \pi \phi^2$ , the surface brightness produced by the volume element is simply

$$db = \frac{df}{d\Omega} = F_\odot^0 e^{-\tau(OP)} n[h(l)] C_{ext}(\lambda) \Phi(\theta) e^{-\tau(OP)} dl$$

and the total surface brightness is finally obtained integrating along the line of sight within the illuminated region:

$$b = \int_{l_0}^{l_1} db dl$$

Finally, to take into account the contribution by the night sky emission, we have added to the computed flux the one implied by the average values measured for Paranal ( $h_s=2.6$  km) and reported by Patat (2003a, Tab. 4). With this, the model is completely constrained and there are no free parameters.

*Acknowledgements.* We wish to thank S.L. Kenyon and J.W.V. Storey for inspiring this work and the ESO Archive Group for the support received during the data retrieval. O.Ugolnikov is supported by a Russian Science Support Foundation grant. Our gratitude goes also to the referee, Dr. A. Tokovinin, for his useful suggestions and comments.

This paper is based on observations made with ESO Telescopes at Paranal Observatory.

#### References

- Adams, C.N., Plass, G.N. & Kattawar, G.W., 1974, *J. Atm. Sci.*, 31, 1662
- Anderson, D.E. & Lloyd, S.A., 1990, *JGR*, 95, 7429
- Blättner, W.G., Horak, H.G., Collins, D.G. & Wells, M.B., 1974, *Applied Optics*, 13, 534
- Chromey, F.R. & Hasselbacher, D.A. 1996, *PASP*, 108, 944
- Divari, N.B. & Plotnikova, L.I., 1966, *Sov. Astron.*, 9, 840
- Ekstrom, P., 2002, *SPIE*, 4815-14
- Roach, F.E. & Gordon J.L., 1973, *The light of the night sky*, (Boston, Dordrecht Reidel)
- Hedin, A.E. 1991, *J. Geophys. Res.* 96, 1159
- Hog, E. et al., 2000, *The Tycho-2 Catalogue on CD-ROM*, Copenhagen University Observatory
- Kenyon, S. L. & Storey, J.W.V., 2005, *PASP*, in press, astro-ph/0511510
- Krisciunas, K. & Schaefer, B.E. 1991, *PASP*, 103, 1033
- Landolt, A. U. 1992, *AJ*, 104, 340
- Lawrence, J.S., Ashley, M.C.B., Tokovinin, A. & Travouillon, T. 2004, *Nature*, 431, 278
- Mateshvili, N., Fussen, D., Vanhellemont, F., Bingen, C., Kyrilä, E., Mateshvili, I. & Mateshvili, G., 2005, *J. Geophys. Res.*, 110, D09209
- McCartney, E.J., 1976, *Optics of the Atmosphere*, (New York, John Wiley & Sons)
- Ougolnikov, O.S. 1999, *Cosmic Research*, 37, n.2, 159
- Ougolnikov, O.S. & Maslov, I.A., 2002, *Cosmic Research*, 40, 224
- Ougolnikov, O.S., Postlyakov, O.V. & Maslov, I.A., 2004, *J. Quant. Spec. Radiat. Transf.*, 88, 233
- Patat, F., 2003a, *A&A*, 400, 1183
- Patat, F., 2003b, *A&A*, 401, 797
- Postlyakov, O.V., 2004, *J. Quant. Spec. Radiat. Transf.*, 88, 297 (the same issue with paper by Ugolnikov, Postlyakov, Maslov).
- Rozenberg, G.V. 1966, *Twilight*, (New York, Plenum Press)

- Smart, W.M., 1977, Textbook on Spherical Astronomy, Sixth Edition,  
(Cambridge, Cambridge University Press)
- Szeifert, T., 2002, FORS1+2 User's Manual, VLT-MAN-ESO-13100-  
1543, Issue 2.3
- Tyson, N.D. & Gal, R. 1993, AJ, 105, 1206
- Wu, B. & Lu, D., 1988, Applied Optics, 27, 4899